

# Broadband Alcock-Paczynski test exploiting redshift distortions

Yong-Seon Song<sup>1</sup>, Teppei Okumura<sup>2</sup> and Atsushi Taruya<sup>3,4</sup>

<sup>1</sup> Korea Astronomy and Space Science Institute, Daejeon 305-348, R. Korea

<sup>2</sup> Institute for the Early Universe, Ewha Womans University, Seoul 120-750, R. Korea

<sup>3</sup> Research Center for Early Universe, School of Science, University of Tokyo, Bunkyo-ku, Tokyo 113-0033, Japan

<sup>4</sup> Yukawa institute for theoretical physics, Kyoto University, Kyoto 606-8502, Japan

8 March 2019

## ABSTRACT

Baryon acoustic oscillations (BAO), known as one of the largest cosmological objects, is now recognized as standard cosmological tool to measure geometric distances via the Alcock-Paczynski effect, by which the observed BAO exhibits characteristic anisotropies in addition to the redshift distortions. This implies that once we know the correct distances to the observed BAO, the tip points of baryon acoustic peaks in the anisotropic correlation function of galaxies,  $\xi(\sigma, \pi)$ , can form a great circle (hereafter 2D BAO circle) in the  $\sigma$  and  $\pi$  plane, where  $\sigma$  and  $\pi$  are the separation of galaxy pair parallel and perpendicular to the line-of-sight, respectively. This 2D BAO circle is indeed robust and remains unchanged under the variations of the unknown galaxy bias and/or coherent motion, while it varies transversely and radially with respect to the variations of  $D_A$  and  $H^{-1}$ , respectively. Hereby the ratio between transverse distance  $D_A$  and the radial distance  $H^{-1}$  uniquely reproduces the intrinsic shape of 2D BAO circle, which is *a priori* given by the known broadband shape of spectra. We dub it as the broadband Alcock-Paczynski test exploiting redshift distortions. All BAO peaks of  $\xi(\sigma, \pi)$  are precisely calculated with the improved theoretical model of redshift distortion. We test the broadband Alcock-Paczynski method using BOSS-like mock catalogues. The transverse and radial distances are probed in precision of several percentage fractional errors, and the coherent motion is observed to match with the fiducial values accurately.

**Key words:** cosmology; large-scale structure

## 1 INTRODUCTION

The observational evidence of “dark energy” with an effective negative pressure has revolutionized cosmology in the last decade. Since the first evidence of dark energy in 1998 (Perlmutter et al. 1999; Riess et al. 1998), there has been substantial observational and theoretical research aimed at understanding the true nature of this phenomenon. In recent years, many authors have started exploring the possibility that dark energy, and the observed acceleration of the expansion of the Universe, could be the consequence of an incomplete theory of gravity on cosmological scales and may require modifications to Einstein’s theory of General Relativity. A prime goal of precision cosmology in the next decades is to provide cosmological observables in a theoretical model independent way for a fair judgement of confirmation or exclusion. In other words, cosmic observation should be unplugged from our prior knowledge of underlying sciences. We study the theoretical model independent observational tool to probe the distance measures and the growth functions through the Alcock-Paczynski test using the anisotropy spectra of redshift distortions.

The full history of cosmic expansion can be reconstructed using galaxy redshift surveys. Despite the enriched nonlinear structures, the zero-th order description of our current universe is ho-

mogeneous and isotropic over sufficiently large scales (York et al. 2000; Peacock et al. 2001; Hawkins et al. 2003; Percival et al. 2004; Zehavi et al. 2005; Tegmark et al. 2006; Guzzo et al. 2008; Drinkwater et al. 2010; Kazin et al. 2010; Reid et al. 2010, 2012). The measured spatial distribution of galaxies is determined by the density fluctuations and the coherent peculiar velocities of galaxies. Even though we expect the clustering of galaxies in real space to have no preferred direction, galaxy maps produced by estimating distances from redshifts obtained in spectroscopic surveys reveal an anisotropic galaxy distribution. The anisotropies arise because galaxy recession velocities, from which distances are inferred, include components from both the Hubble flow and peculiar velocities driven by the clustering of matter. Measurements of the anisotropies allow constraints to be placed on the rate of growth of clustering and Hubble flow along the line of sight (Wang 2006; Gaztanaga, Cabre & Hui 2009; Padmanabhan & White 2008; White, Song & Percival 2009; Song 2011; Taruya, Saito & Nishimichi 2011; Chuang & Wang 2012; Reid et al. 2012; Beutler et al. 2012; Zhang, Pan & Zheng 2013)

The observed spectra in redshift space depend not only on fluctuations of density and velocity fields but also on distance measures of components perpendicular and parallel to the line of sight (Blake & Glazebrook 2003; Seo & Eisenstein 2003). Unfor-

unately, those are not simultaneously decomposed out of redshift distortions due to high degeneracy among observables. We can, in principle, resolve this problem if we understand the shape of the power spectrum precisely. In the context of standard cosmology, the shape of spectra is determined before the last scattering surface, and in linear theory, it evolves coherently through all scales. In this case, the shape of spectra is determined by CMB experiments, both the coherent growth functions of density and velocity and the distance measures can be determined separately in precision using the Alcock–Paczynski test in Fourier space (Song 2013).

In this paper, we present the Alcock–Paczynski test in the configuration space where galaxy clustering is described by correlation function of  $\xi(\sigma, \pi)$ . If we connect all tip points of BAO peaks observed in  $\xi(\sigma, \pi)$ , it forms a great circle which is called as 2D BAO circle (Hu & Haiman 2003; Matsubara 2004). The shape of spectra is assumed to be determined at the last scattering surface by CMB experiments. Then the 2D BAO circle becomes invariant to the variation of either density or velocity growth function. However, the 2D BAO circle is altered transversely to the variation of the angular diameter distance  $D_A$ , and radially to the variation of the inverse of Hubble rate  $H^{-1}$ . This feature enables us to measure both transverse and radial distances simultaneously with structure formation. Hereby we dub this method as the broadband Alcock–Paczynski test. Note that the use of the broadband shape of correlation function or power spectrum in the Alcock–Paczynski test has been already advocated before (e.g., Ballinger, Peacock & Heavens 1996; Matsubara & Suto 1996; Magira, Jing & Suto 2000), but these previous works have mainly focused on the cases with featureless initial spectrum. Taking account of the BAO as standard ruler, the broadband Alcock–Paczynski test can give a much more impact on the precision estimation of geometric distances.

The observed  $\xi(\sigma, \pi)$  from redshift distortion maps have been plagued by systematic uncertainties which have made their cosmological constraints uncompetitive compared to other probes of the Universe. The cosmological density and velocity field couple together and evolve nonlinearly. In addition, the mapping formula between the real and redshift space is intrinsically nonlinear. These nonlinearities prevent us from inferring the linear coherent motion from the redshift space clustering straightforwardly. Recently, an accurate theoretical model for the redshift distortion was proposed in (Taruya, Nishimichi & Saito 2010). They take into account the fact that the linear squeezing and non-linear smearing effects on distorted maps are not separable to each other and develop a more elaborate description than simple factorized formulation. The derived correction terms at next-to-leading orders assist us to achieve better fit to simulated data of dark matter. They also include non-linear corrections computed with the closure approximation to predict the non-linear growth in density–density, density–velocity and velocity–velocity spectra (Taruya & Hiramoto 2008; Taruya, Saito & Nishimichi 2011). In our previous work (Song et al. 2013), we successfully decompose both density and velocity spectra in Fourier space using the improved model of redshift distortions. In this work, we find that BAO peaks observed in  $\xi(\sigma, \pi)$  are precisely reproduced as well in the configuration space using the same method. Accordingly, both  $D_A$  and  $H^{-1}$  are measured in accuracy.

Despite all theoretical efforts, the exact form of FoG effect is unknown. We adopt most common functional form of FoG effect, such as Gaussian, and parameterize FoG effect using one-dimensional velocity dispersion representing the randomness of the motion which erases the correlation structure on small scales. The parameter space is extended to include this uncertainty of

FoG effect in addition to the linear spectra of density and velocity fields, which were originally proposed by (Song & Kayo 2010; Tang, Kayo & Takada 2011). This unknown factor limits the detectability of observables significantly. But, when  $\xi(\sigma, \pi)$  is observed in the binned space of  $\sigma$  and  $\pi$ , this non-perturbative effect can be handled by eliminating bins which are highly contaminated by non-linear physics. We apply the appropriate bounds of cut-off for the treatment of the analysis.

We test our new broadband Alcock–Paczynski test as a tool to measure  $D_A$ ,  $H^{-1}$ , and the growth function of coherent motion using 611 BOSS mocking catalogues at  $z = 0.57$ . Those observables are marginalized with unknown galaxy bias and non-perturbative FoG effect. The results indicate that the precise measurements of  $D_A$ ,  $H^{-1}$ , and the growth function of coherent motion are possible by our treatment. Here are layouts of the paper. In section 2, we introduce the improved model of redshift distortions. In section 3, we introduce the mock catalogues which we use. In section 4, we explain the broadband Alcock–Paczynski test. In section 5 and 6, results and conclusion are presented.

## 2 THE THEORETICAL MODEL OF REDSHIFT DISTORTIONS

### 2.1 Needs for improved theoretical model

As we mentioned in Sec. 1, the redshift–space two–point correlation function of mass tracers,  $\xi_s$ , exhibits anisotropies mainly due to the peculiar motions of galaxies (Kaiser 1987), and is described as a function of  $\sigma$  and  $\pi$ , where  $\sigma$  and  $\pi$  are the separations between the mass tracers perpendicular and parallel to the line-of-sight direction, respectively. Typically, for the separation along the line of sight (i.e.,  $\sigma \simeq 0$ ), the clustering in redshift space shows an elongated structure, and the resultant redshift-space correlation function is compressed or suppressed. At small separation, the suppression appears due to the nonlinear velocity dispersions of galaxies, known as Finger of God effect, while the compression in correlation function becomes manifest at large separation, and the clustering pattern is squashed by the coherent infalls toward overdense regions, called Kaiser effect.

In the linear regime of gravitational instability, the density and velocity fields are coherently evolved through the continuity equation. This is exactly the situation characterized by the Kaiser effect, and the redshift-space correlation function  $\xi_s(\sigma, \pi)$  is uniquely mapped from the real-space correlation function  $\xi(r)$ , which is computed with the linear theory of gravitational instability (Lilje & Efstathiou 1989; McGill 1990; Lahav et al. 1991; Hamilton 1992; Fisher, Scharf & Lahav 1994). Note that the commonly used streaming model (Fisher 1995), in which the function  $\xi_s$  is given by the convolution of real-space correlation function with velocity distribution function, also recovers the Kaiser limit of redshift-space correlation in the the large-scale limit. It is, however, important to note that the resultant correlation function  $\xi_s(\sigma, \pi)$  differs from the real-space correlation function for all configurations, even those perpendicular to the line of sight (e.g., (Soccimarro 2004)). This is in marked contrast to the redshift-space power spectrum.

In our previous work (Song et al. 2013), as a simple theoretical model, the linear squashing effect is combined in a multiplicative way with the Gaussian damping function characterizing the Finger of God (hereafter FoG) effect. In comparing it with the measured correlation function at  $\sigma < 60 h^{-1}$  Mpc and

$\pi < 40 h^{-1}$  Mpc, the cut-off strategy is applied to eliminate bins in non-linear regime at which the theoretical model of the redshift distortions is broken down. Then the rest of bins at large separations successfully fits to the theory, and provides us coherent motions at low redshifts.

Recently, BOSS released new data, and with this data set, it is now able to uncover the correlation function  $\xi_s(\sigma, \pi)$  at larger  $\sigma$  and  $\pi$ , where 2D BAO structure is clearly visible. This implies that making full use of Alcock–Paczynski effect, we may simultaneously measure the geometric distance and the coherent motion field. However, it turned out that measurements of coherent motion from redshift distortion maps suffers from the nonlinear systematic effects. While the BAO basically lies at the scales close to the linear regime, because of the nonlinear gravitational evolution, the small peak structure of BAO tends to be smeared out. Further, the cosmological density and velocity fields couple together, and they evolve nonlinearly. Then, due to its nonlinear nature of the mapping formula between the real and redshift space, the resultant correlation function can get a noticeable nonlinear correction even at BAO scales. Hence, in order to unlock the full cosmological power of the BAO as well as the redshift distortions, a simple factorized model of redshift-space correlation function is insufficient to describe the measured 2D BAO structure, and we need a more elaborate description, for which we will discuss below.

## 2.2 The improved theoretical spectra in Fourier space

Before presenting an improved model of correlation function, let us first consider the redshift-space power spectrum. On large scales, the observed large-scale structure is basically described by a small perturbation to the homogeneous universe. Ignoring the higher-order contributions, the two-dimensional power spectrum in redshift space,  $\tilde{P}(k, \mu)$ , given as the function of wavenumber  $k$  and directional cosine  $\mu$  between line-of-sight direction and  $k$ , is solely characterized by the Kaiser effect, and can be expressed as Kaiser (1987)

$$\tilde{P}(k, \mu) = P_{\delta\delta}^{\text{lin}}(k) + 2\mu^2 P_{\delta\Theta}^{\text{lin}}(k) + \mu^4 P_{\Theta\Theta}^{\text{lin}}(k). \quad (1)$$

As we mentioned, the observed redshift-space power spectra suffers significantly from nonlinear corrections even at large scales. One important effect is the gravitational evolution. Further, the random motion of galaxies is known to cause the FoG effect. The approximate prescription to describe these nonlinear effects was proposed by Scoccimarro, and it is expressed as (Scoccimarro 2004)

$$\tilde{P}(k, \mu) = \{P_{\delta\delta}(k) + 2\mu^2 P_{\delta\Theta}(k) + \mu^4 P_{\Theta\Theta}(k)\} G^{\text{FoG}}(k\mu\sigma_p). \quad (2)$$

where  $\sigma_p$  is the one-dimensional velocity dispersion. Nonlinear corrections due to the random motion is described by the factor  $G^{\text{FoG}}$  which is given in the Gaussian function,

$$G^{\text{FoG}}(k\mu\sigma_p) = \exp\left\{-\frac{1}{2}(k\mu\sigma_p)^2\right\}, \quad (3)$$

The auto- and cross-power spectra of the two fields expressed as  $P_{XY}^{\text{lin}}(k)$ , with  $X$  and  $Y$  being either  $\delta$  or  $\Theta$ , are the nonlinear generalization of the linear counterpart  $P_{XY}^{\text{lin}}(k)$  in Eq. 1. With the model given by Eq. 2, the prediction of redshift-space correlation function  $\xi(\sigma, \mu)$  reproduces reasonably well the anisotropic clustering structure at scales of  $\sigma < 60 h^{-1}$  Mpc and  $\mu < 30 h^{-1}$  Mpc. However, it fails to match the observed 2D BAO peak structure.

Beyond a simple model prescription, one crucial aspect of the redshift distortions may be that the linear squeezing and nonlinear smearing effects on distorted maps are not separately treated. Taking account of this fact, Taruya, Nishimichi

& Saito (Taruya, Nishimichi & Saito 2010) proposed an improved model of the redshift-space power spectrum, in which the coupling between the density and velocity fields associated with the Kaiser and the FoG effects is perturbatively incorporated into the power spectrum expression. The resultant expression looks similar to Eq. 2, but includes nonlinear corrections consisting of higher-order polynomials (Taruya, Nishimichi & Saito 2010):

$$\tilde{P}(k, \mu) = \{P_{\delta\delta}(k) + 2\mu^2 P_{\delta\Theta}(k) + \mu^4 P_{\Theta\Theta}(k) + A(k, \mu) + B(k, \mu)\} G^{\text{FoG}}. \quad (4)$$

Here the  $A(k, \mu)$  and  $B(k, \mu)$  terms are the nonlinear corrections, and are expanded as power series of  $\mu$ , including the powers up to  $\mu^6$  for the  $A$  term and  $\mu^8$  for the  $B$  term. In this paper, adopting the model given in Eq. 4, we will proceed to the cosmological analysis, and investigate the impact of these nonlinear corrections.

In computing the power spectrum, we need to properly take into account the effect of nonlinear gravitational evolution not only for the  $A$  and  $B$  terms but also for the auto- and cross-power spectra  $P_{XY}(k)$ . Since the standard perturbation theory is known to produce ill-behaved expansion leading to the bad UV behavior, a consistent calculation of correlation function should be made with the improved perturbation theory with an appropriate UV regularization. Here, we apply the resummed perturbation theory called RegPT (Taruya et al. 2012), and following the prescription described in Taruya, Nishimichi & Bernardeau (2013), we compute the power spectra  $P_{XY}(k)$  as well as the  $A$  and  $B$  terms, including the nonlinear corrections up to the two-loop order, i.e., next-to-next-leading order. Note that the RegPT scheme is based on a multipoint propagator expansion, and with this scheme, any statistical quantities consisting of density and velocity fields are built up with multipoint propagators, in which non-perturbative properties of gravitational growth are wholly encapsulated (Bernardeau, Crocce & Scoccimarro 2008). Making use of the analytic properties of the propagators, a novel regularized treatment has been implemented (Bernardeau, Crocce & Scoccimarro 2012), showing that the proposed scheme can be used to give a percent-level prediction of power spectrum and correlation function at weakly nonlinear regime in both real and redshift spaces (Taruya et al. 2012; Taruya, Nishimichi & Bernardeau 2013).

With the RegPT scheme, we pre-compute the nonlinear corrections to the auto- and cross-power spectra  $P_{XY}$  in the fiducial cosmological model:

$$\delta P_{XY}^{\text{fid}}(k) = P_{XY}^{\text{fid}}(k) - P_{XY}^{\text{fid,lin}}(k). \quad (5)$$

Adding up linear and nonlinear parts, we have

$$P_{XY}(k) = \frac{G_X(z) G_Y(z)}{G_X^{\text{fid}}(z) G_Y^{\text{fid}}(z)} \{P_{XY}^{\text{fid,lin}}(k) + \delta P_{XY}^{\text{fid}}(k)\}. \quad (6)$$

Here, the prefactor  $G_X(z)$  includes the information on the structure growth and galaxy bias, which will be later clarified in Sec. 4.1. Strictly speaking, the second term depends on not only the linear power spectrum  $\delta_{XY}^{\text{fid}}$  but also the cosmological model as well as the gravity theory.

To sum up, we adopt the redshift-space power spectrum,  $\tilde{P}(k, \mu)$ , given in Eq. 4, which can be recast as:

$$\tilde{P}(k, \mu) = \sum_{n=0}^8 Q_{2n}(k) \mu^{2n} G^{\text{FoG}}(k\mu\sigma_p), \quad (7)$$

Here,  $\sigma_p$  is the free parameter which we allow to float in the cosmological analysis. Although this may lead to an additional uncertainty in the parameter estimation, our previous analysis suggests

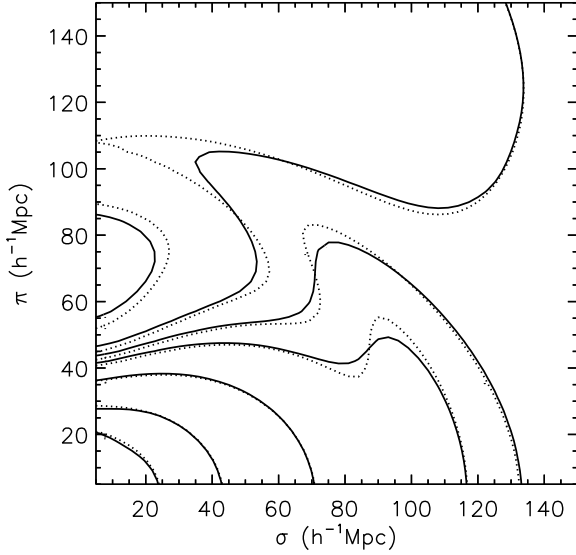


**Figure 1.** Dash contours represent the theoretical  $\xi(\sigma, \pi)$  of the simple combination of Kaiser model and Gaussian FoG effect. Solid contours represent the improved  $\xi(\sigma, \pi)$ . The level of  $\xi_s(\sigma, \pi)$  is (0.2, 0.06, 0.16, 0.005, 0.002, -0.001, -0.006) from the inner to outer contours.

that as long as we consider the weakly nonlinear scales, cosmological analysis can be made independently of the functional form of FoG effect. The functions  $Q_n$  are given by

$$\begin{aligned}
 Q_0(k) &= P_{\delta\delta}^{\text{lin}}(k) + \delta P_{\delta\delta}(k), \\
 Q_2(k) &= 2P_{\delta\delta}^{\text{lin}}(k) + 2\delta P_{\delta\delta}(k) + C_2(k), \\
 Q_4(k) &= P_{\Theta\Theta}^{\text{lin}}(k) + \delta P_{\Theta\Theta}(k) + C_4(k), \\
 Q_6(k) &= C_6(k), \\
 Q_8(k) &= C_8(k),
 \end{aligned} \tag{8}$$

where  $C_n$  includes the nonlinear correction terms  $A$  and  $B$ , and we assume the perfect correlation between linear density and velocity fields, i.e.,  $P_{\Theta\Theta}^{\text{lin}}(k) = [P_{\delta\delta}^{\text{lin}}(k)P_{\Theta\Theta}^{\text{lin}}(k)]^{1/2}$ . Apart from linear-order quantities, nonlinear contributions in each term are computed with the RegPT scheme, consistently including the perturbative corrections up to the two-loop order.

### 2.3 The improved correlation $\xi(\sigma, \pi)$ in configuration space

Once provided the power spectrum, it is now rather easy task to compute the correlation function. The redshift-space correlation function  $\xi(\sigma, \mu)$  is generally expanded as

$$\begin{aligned}
 \xi^s(\sigma, \pi) &= \int \frac{d^3k}{(2\pi)^3} \tilde{P}(k, \mu) e^{i\mathbf{k}\cdot\mathbf{s}} \\
 &= \sum_{\ell: \text{even}} \xi_\ell(s) \mathcal{P}_\ell(\nu),
 \end{aligned} \tag{9}$$

with  $\mathcal{P}$  being the Legendre polynomials. Here, we define  $\nu = \pi/s$  and  $s = (\sigma^2 + \pi^2)^{1/2}$ . The moments of correlation function,  $\xi_\ell(s)$ , are defined by,

$$\xi_\ell(s) = i^\ell \int \frac{k^2 dk}{2\pi^2} \tilde{P}_\ell(k) j_\ell(ks). \tag{10}$$

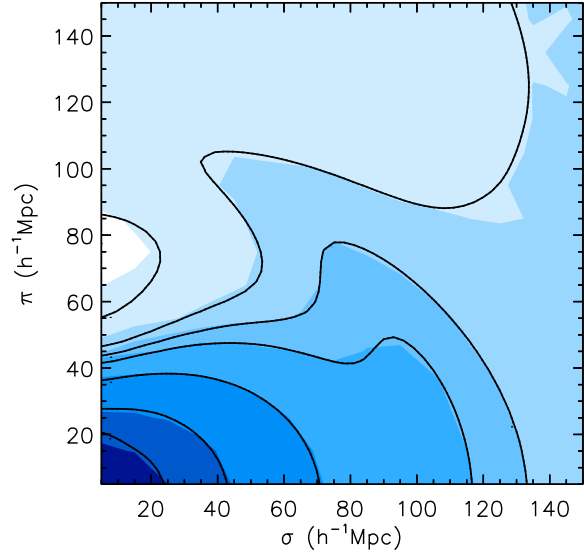


**Figure 2.** We compare the observed and the theoretical  $\xi(\sigma, \pi)$ . The dotted red contours represent the observed  $\xi(\sigma, \pi)$  using simulated maps. The black contour in the left panel represents the theoretical  $\xi(\sigma, \pi)$  without using  $\delta P_{XY}$  and  $C_n$ , and the black contour in the right panel represents the theoretical  $\xi(\sigma, \pi)$  using theoretical models described in Section 2.

For the improved model given in Eq. 7, the multipole power spectra  $\tilde{P}_\ell(k)$  are explicitly given by,

$$\begin{aligned}
 \tilde{P}_0(k) &= p_0(k), \\
 \tilde{P}_2(k) &= \frac{5}{2} [3p_1(k) - p_0(k)], \\
 \tilde{P}_4(k) &= \frac{9}{8} [35p_2(k) - 30p_1(k) + 3p_0(k)], \\
 \tilde{P}_6(k) &= \frac{13}{16} [231p_3(k) - 315p_2(k) + 105p_1(k) - 5p_0(k)], \\
 \tilde{P}_8(k) &= \frac{1}{64} [6435p_4(k) - 12012p_3(k) + 6930p_2(k) \\
 &\quad - 1260p_1(k) + 35p_0(k)],
 \end{aligned} \tag{11}$$

where we define the function  $p_m(k)$ :

$$p_m(k) = \frac{1}{2} \sum_{n=0}^4 \frac{\gamma(m+n+1/2, \kappa)}{k^{m+n+1/2}} Q_{2n}(k) \tag{12}$$

with  $\kappa = k^2 \sigma_p^2$ . The function  $\gamma$  is the incomplete gamma function of the first kind:

$$\gamma(n, \kappa) = \int_0^\kappa dt t^{n-1} e^{-t}. \tag{13}$$

In Fig. 1, we plot the redshift-space correlation function in  $(\sigma, \pi)$ -plane, and compare the improved model based on the expression 4 (or Eq. 7) with simple Scoccimarro's model given in Eq. 2. Dashed contours represent the result of the simple combination of Kaiser and Gaussian FoG effects, while solid contours represent the improved model prediction. Here, in both cases, the constant bias parameter and the velocity dispersion parameter  $\sigma_p$  are set to the best-fitting values obtained from the cosmological analysis with Mock catalog (see Table 1). At the scales accessible to the previous SDSSII, i.e.,  $\sigma < 60 h^{-1}$  Mpc and  $\pi < 40 h^{-1}$  Mpc, both theoretical

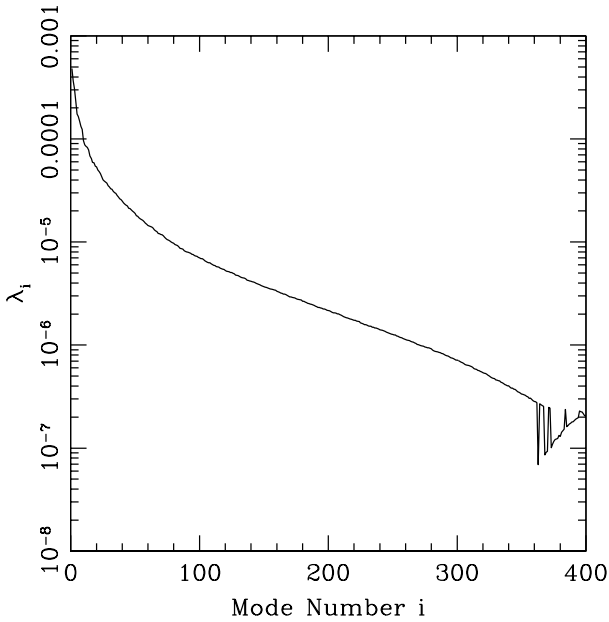


**Figure 3.** Eigenvalues for the covariance matrix for the measurement of the correlation function of the CMASS galaxy mock catalogs.

models agree to each other beyond the cut-off scales. At larger scales,  $\sigma < 150 h^{-1} \text{Mpc}$  and  $\pi < 150 h^{-1} \text{Mpc}$ , however, there appears noticeable discrepancy between both descriptions. Differences are particularly manifest around the baryon acoustic peak. Note that in computing the improved model, the contribution from the  $Q_8$  term turns out to be small in correlation function, and no serious difference appears if we neglect such a higher-order polynomial. Hence, in the analysis below, we drop the  $Q_8$  term and compute the correlation function.

### 3 MEASUREMENTS

#### 3.1 Measured correlation function from mock catalogs

In order to check the validity of our improved model in Sec. 2, we first present the redshift-space correlation function  $\xi_s(\sigma, \pi)$  measured from a mock galaxy sample. We use the mock galaxy catalogs created by Manera et al. (2013), which is designed to investigate the various systematics in a galaxy sample from Data Release 9 (DR9) of the Baryon Oscillation Spectroscopic Survey (BOSS) (Schlegel, White & Eisenstein 2009; Eisenstein et al. 2011; Anderson et al. 2012), referred to as ‘‘CMASS’’ galaxy sample. In constructing the mock galaxy catalog, Manera et al. (2013) utilized second-order Lagrangian perturbation theory (2LPT) for the galaxy clustering driven by gravity, and thus it enables to create a mock catalog much faster than running an  $N$ -body simulation. The redshift range of galaxies in the catalog is  $0.47 < z < 0.7$  and each catalog contains  $\sim 2.67 \times 10^5$  galaxies, 90% of which are central galaxies residing in dark matter halos of  $\sim 10^{13} h^{-1} M_\odot$ . We analyze 611 realizations of those mock CMASS catalogs.

We measure the two-dimensional redshift-space correlation function using the Landy-Szalay estimator (Landy & Szalay 1993):

$$\xi_s(\sigma, \pi) = \frac{DD - 2DR + RR}{RR}, \quad (14)$$

where  $DD$ ,  $RR$ , and  $DR$  are the normalized counts of galaxy-galaxy,

random-random, and galaxy-random pairs, respectively, in a particular bin in the space of  $(\sigma, \pi)$ . The random catalog, which was also created by Manera et al. (2013), contains  $1.76 \times 10^6$  points as galaxies with no influence of gravitational clustering.

The resulting redshift-space correlation function measured from the mock catalogs, after averaging over all realizations, is shown in Fig. 2. The filled blue contours are the measured correlation function, which is pixelized into rectangular cells with  $\Delta\sigma = \Delta\pi = 10 h^{-1} \text{Mpc}$ . The contour is essentially the same as figure 3 of Reid et al. (2012), where they used the observed data of CMASS galaxies. Note that the ridge structure seen at scales around  $\sim 105 h^{-1} \text{Mpc}$  is the two-dimensional feature of baryon acoustic oscillations (BAO) (Matsubara 2004), which has been already detected for several observational data (Okumura et al. 2008; Gaztanaga, Cabre & Hui 2009; Kazin et al. 2010; Reid et al. 2012).

In Fig. 2, we also show the improved model prediction of  $\xi(\sigma, \pi)$ , depicted as solid contours. The improved model successfully describes the ridge structure, which is somewhat smeared out due to the nonlinear effects of gravity and redshift distortions. This fact implies that with the improved model of correlation function, we can handle the broad-band shape of the correlation function. It enables us to put a tighter constraint on the geometric distances through the Alcock-Paczynski effect, which we will discuss in next section.

#### 3.2 Covariance matrix

Because there are strong correlations between different bins of the correlation function  $\xi_s(\sigma, \pi)$ , it is necessary to estimate a covariance matrix. Jackknife resampling (Lupton 1993), which is straightforward to perform and thus is often adopted, tends to underestimate cosmic variance at BAO scales we are interested in. Since we want to analyze the full two-dimensional map that has much larger degree-of-freedom, we need hundreds of independent realizations in order to have the non-singular covariance matrix. In our analysis we use the mock CMASS catalogs directly in order to estimate the covariance matrix because the total number of the catalogs, 611, is large enough. In fact the mock catalogs were created for the purpose of estimating the covariance. However, in previous works different statistics which have smaller degree of freedom were used, e.g., multipoles (Reid et al. 2012).

Using the correlation function computed from each of the 611 mock catalogs, we estimate a covariance matrix as

$$\text{Cov}(\xi_i, \xi_j) = \frac{1}{N-1} \sum_{k=1}^N [\xi_k(\mathbf{r}_i) - \bar{\xi}(\mathbf{r}_i)][\xi_k(\mathbf{r}_j) - \bar{\xi}(\mathbf{r}_j)], \quad (15)$$

where  $N = 611$ ,  $\xi_k(\mathbf{r}_i)$  represents the value of the correlation function of  $i$ th bin of  $(\sigma, \pi)$  in  $k$ th realization, and  $\bar{\xi}(\mathbf{r}_i)$  is the mean value of  $\xi_k(\mathbf{r}_i)$  over realizations. We can then obtain the normalized covariance matrix as

$$C_{ij} = \frac{\text{Cov}(\xi_i, \xi_j)}{\sqrt{\text{Cov}(\xi_i, \xi_i)\text{Cov}(\xi_j, \xi_j)}}. \quad (16)$$

In order to reduce the statistical noise in our covariance matrix, we perform a single value decomposition (SVD) of the matrix as done in Song et al. (2010, 2011),

$$C_{ij} = U_{ik}^\dagger D_{kl} V_{lj}, \quad (17)$$

where  $U$  and  $V$  are orthogonal matrices that span the range and the null space of  $C_{ij}$  and  $D_{kl} = \lambda^2 \delta_{kl}$ , a diagonal matrix with singular values along the diagonal.

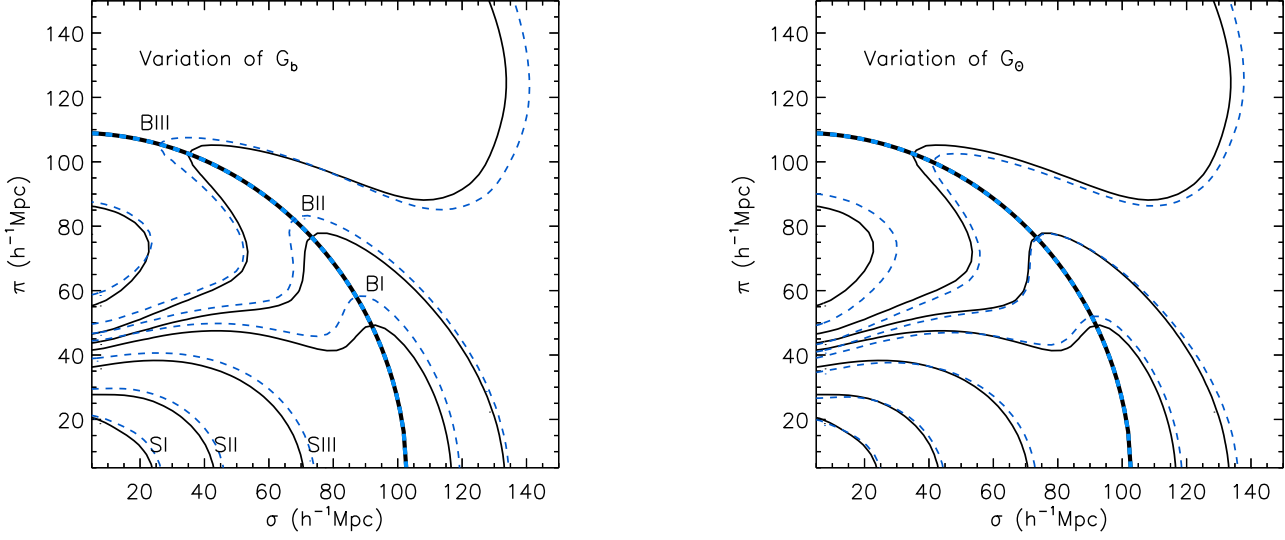


**Figure 4.** (*Left panel*) Thin black solid curves represent the contours of fiducial  $\xi(\sigma, \pi)$  with the same levels in Fig.1. Three inner curves labeled by SI, SII and SIII represent the contours without BAO peaks, and three outer curves labeled by BI, BII and BIII represent the contour with BAO peaks. Thick black solid curve represents the fiducial 2D BAO circle on which all BAO peaks are located. Thin blue dash curves represent the contours of  $\xi(\sigma, \pi)$ , when we vary  $G_b$  by 10%. Thick blue dash curve represents the 2D BAO circle with variation of  $G_b$ . (*Right panel*) Thin black solid curves represent the contours of fiducial  $\xi(\sigma, \pi)$  with the same levels in Fig.1. Thick black solid curve represents the fiducial 2D BAO circle on which all BAO peaks are located. Thin blue dash curves represent the contours of  $\xi(\sigma, \pi)$ , when we vary  $G_\theta$  by 10%. Thick blue dash curve represents the 2D BAO circle with variation of  $G_\theta$ .

In Fig. 3, we show the eigenvalues ( $\lambda_i$ ) for the increasing eigenmodes. Since higher-order modes are dominated by noise, we will truncate such eigenmodes as seen in next section.

#### 4 STATISTICAL METHOD TO TEST ALCOCK–PACZYNSKI EFFECT USING 2D BAO

##### 4.1 Fitting parameters

The observed clustering in redshift space is known as a probe of structure formation of density and velocity fields. In addition, it can be a tracer to determine both transverse and radial distances exploiting Alcock–Paczynski effect (Blake & Glazebrook 2003; Seo & Eisenstein 2003; Wang 2006; Song et al. 2011; Chuang & Wang 2012; Beutler et al. 2012). Unfortunately, there is significant degeneracy among unknowns. None of observables are measured in precision, unless the specific condition is imposed *a priori*. Couple of approaches are proposed to break this degeneracy in Song (2013); one is the treatment to give a broadband prior on the shape of spectra determined by CMB experiments, and the other is the treatment to unify the transverse distance with the radial distance based upon the assumption of FLRW universe prior. Here, we investigate the approach with the given broadband shape prior.

In the context of standard cosmology, the shape of spectra is determined before the last scattering surface, and in linear theory, it evolves coherently through all scales. The history of structure formation evolution is divided into two regimes; epochs before matter-radiation equality ( $a_{eq}$ ) and a later epoch of coherent evolution of unknown effect on structure formation from new physics. We can then express various power spectra of the density field splits into these two epochs, with the shape-dependent part determined by

knowledge of our standard cosmology, and the coherent evolution part only affected by new physics. Mathematically, this is written as,

$$\begin{aligned} P_{\Phi\Phi}(k, a) &= D_\Phi(k)g_\Phi^2(a), \\ P_{bb}(k, a) &= D_m(k)g_b^2(a), \\ P_{\Theta_m\Theta_m}(k, a) &= D_m(k)g_{\Theta_m}^2(a), \end{aligned} \quad (18)$$

where  $\Phi$  denotes the curvature perturbation in the Newtonian gauge,

$$ds^2 = -(1 + 2\Psi)dt^2 + a^2(1 + 2\Phi)dx^2. \quad (19)$$

These power spectra are then partitioned into a scale-dependent part ( $D_\Phi(k), D_m(k)$ ) and a scale-independent (coherent evolution) component ( $g_\Phi, g_b, g_{\Theta_m}$ ). We define here  $g_b = b g_{\delta_m}$  where  $b$  is the standard linear bias parameter between galaxy (or cluster) tracers and the underlying dark matter density. The expression of  $D_\Phi(k)$  and  $D_m(k)$  is available in citation, and assumed to be given by CMB experiments precisely. The  $D_m(k)$  is determined by the fiducial cosmological parameters.

Unlike the shape part, the coherent evolution component,  $g_\Phi, g_b$  and  $g_{\Theta_m}$  are not generally parameterized by known standard cosmological parameters. We thus normalize these growth factors at  $a_{eq}$  such that,

$$\begin{aligned} g_\Phi(a_{eq}) &= 1, \\ g_{\delta_m}(a_{eq}) &= a_{eq}g_\Phi(a_{eq}), \\ g_{\Theta_m}(a_{eq}) &= -\frac{dg_{\delta_m}(a_{eq})}{d \ln a}. \end{aligned} \quad (20)$$

Instead of determining growth factors using cosmological parameters, we measure these directly in a model-independent way at the given redshift without referencing to any specific cosmic acceleration model and with the minimal assumption of coherent evolution

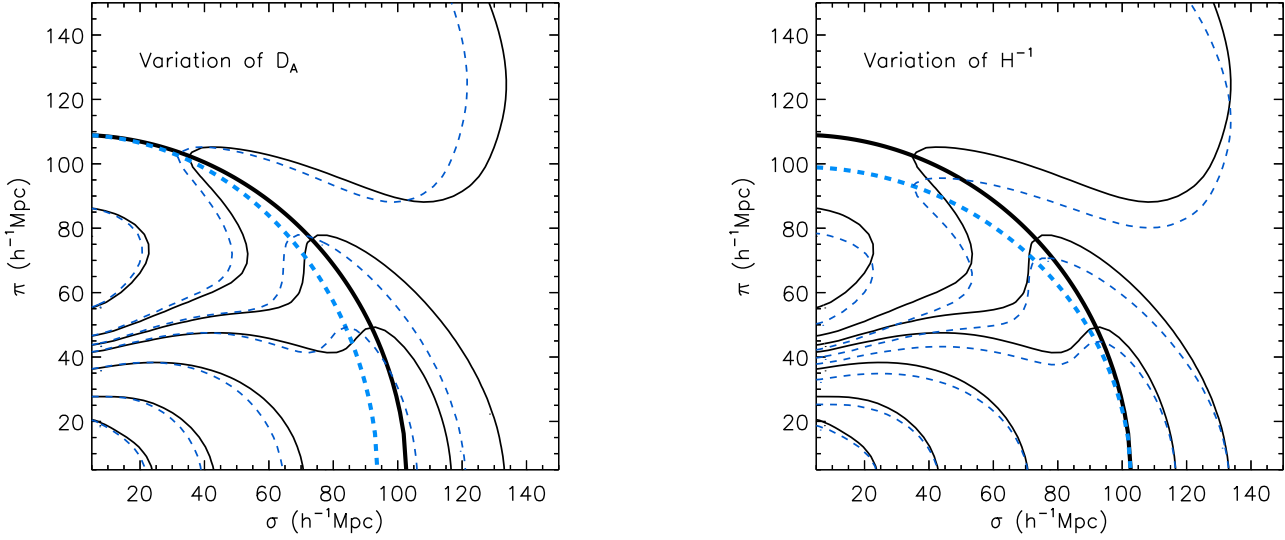


**Figure 5.** (Left panel) Thin black solid curves represent the contours of fiducial  $\xi(\sigma, \pi)$  with the same levels in Fig.1. Thick black solid curve represents the fiducial 2D BAO circle on which all BAO peaks are located. Thin blue dash curves represent the contours of  $\xi(\sigma, \pi)$ , when we vary  $D_A$  by 10%. Thick blue dash curve represents the 2D BAO circle with variation of  $D_A$ . (Right panel) Thin black solid curves represent the contours of fiducial  $\xi(\sigma, \pi)$  with the same levels in Fig.1. Thick black solid curve represents the fiducial 2D BAO circle on which all BAO peaks are located. Thin blue dash curves represent the contours of  $\xi(\sigma, \pi)$ , when we vary  $H^{-1}$  by 10%. Thick blue dash curve represents the 2D BAO circle with variation of  $H^{-1}$ .

of modes after  $a_{eq}$ . Considering the uncertainty in the determination of initial spectra,  $A_S^2$ , from the CMB anisotropy, which is degenerate with the optical depth of re-ionization, we combine both  $A_S^2$  and  $g_X$  (where  $X$  denotes each component of  $\Phi$ ,  $b$  and  $\Theta_m$ ) with proper scaling for convenience as  $G_X = g_X A_S / A_S^*$ . Our result on measuring the coherent motion is independent of our choice of an arbitrary constant  $A_S^{*2}$ . The normalized density and coherent motion growth functions are given by  $G_b$  and  $G_\Theta$ .

The transverse and radial distance components are given by  $D_A$  and  $H^{-1}$ . Each galaxy is located using angular coordinates and redshift in galaxy redshift surveys. Because the clustering function of  $\xi(\sigma, \pi)$  is measured in comoving distances, the fiducial cosmology should be applied to generate maps in comoving space. The transformation depends on the transverse and radial distances. Instead of recreating maps in comoving space, we obtain the approximate fiducial maps by rescaling the transverse and radial distances. This Alcock–Paczynski effect is described by the relation between  $(D_A^{\text{fid}}, H^{-1 \text{ fid}})$  and  $(D_A^{\text{fit}}, H^{-1 \text{ fit}})$ , where ‘fid’ and ‘fit’ denote the fiducial and fitting distances. The distance measures  $\sigma^{\text{fit}}$  and  $\pi^{\text{fit}}$  are transformed into the fiducial space as,

$$\begin{aligned} \sigma^{\text{fid}} &= \frac{D_A^{\text{fid}}}{D_A^{\text{fit}}} \sigma^{\text{fit}} \\ \pi^{\text{fid}} &= \frac{H^{-1 \text{ fid}}}{H^{-1 \text{ fit}}} \pi^{\text{fit}}. \end{aligned} \quad (21)$$

Accordingly,

$$\begin{aligned} s^{\text{fid}} &= \sqrt{\left(\frac{D_A^{\text{fid}}}{D_A^{\text{fit}}}\right)^2 \sigma^{2 \text{ fit}} + \left(\frac{H^{-1 \text{ fid}}}{H^{-1 \text{ fit}}}\right)^2 \pi^{2 \text{ fit}}} \\ \mu^{\text{fid}} &= \left(\frac{H^{-1 \text{ fid}}}{H^{-1 \text{ fit}}}\right) \pi^{\text{fit}} / \sqrt{\left(\frac{D_A^{\text{fid}}}{D_A^{\text{fit}}}\right)^2 \sigma^{2 \text{ fit}} + \left(\frac{H^{-1 \text{ fid}}}{H^{-1 \text{ fit}}}\right)^2 \pi^{2 \text{ fit}}}. \end{aligned} \quad (22)$$

The measured  $\xi^{\text{fid}}$  is given in the fiducial parameter space with  $(D_A^{\text{fid}}, H^{-1 \text{ fid}})$ , but the correlation function is calculated in the fitting parameters space with  $(D_A^{\text{fit}}, H^{-1 \text{ fit}})$ . The theoretical  $\xi$  with arbitrary  $(D_A, H^{-1})$  is fitted to  $\xi^{\text{fid}}$  using rescaling in the above equations.

The spectra of the density and the velocity fields are naturally expected to receive nonlinear corrections. One of those corrections come from the random motion of galaxies, which results in the damping effect of the power spectrum amplitude. The Gaussian type of FoG function in Eq. 3 is applied in this work. While the shape of FoG effect is given, the one-point PDF of the velocity  $\sigma_p$  is set to be free parameter. We do not understand fully these non-perturbative damping effects at this time. Although we are not able to describe redshift distortions at much smaller scales, we vary  $\sigma_p$  to fit data sets in which the leading order contribution of FoG is dominant.

In summary, we have  $G_b$  and  $G_\Theta$  to describe growth functions,  $D_A$  and  $H^{-1}$  to fit distance measures, and  $\sigma_p$  to model FoG effect. The shape of linear spectra and the form of FoG are assumed to be given by CMB experiments.

## 4.2 The broadband Alcock–Paczynski test

We present  $\xi(\sigma, \pi)$  contours in the left panel of Fig. 4. Three inner curves labeled by SI, SII and SIII represent  $\xi(\sigma, \pi)$  contours without BAO peaks. The levels of contours are  $\xi(\sigma, \pi) = 0.2, 0.06$  and  $0.16$ . Three outer curves labeled by BI, BII and BIII represent  $\xi(\sigma, \pi)$  contours with BAO peaks. The levels of contours are  $\xi(\sigma, \pi) = 0.005, 0.002$  and  $-0.001$ . We connect all tip points of B-type contours to define the 2D BAO circle which is presented as the thick black solid curve in the Figure. In this subsection, the variation of the 2D BAO circle is presented in detail.

The growth function  $G_b$  is a dominant parameter of  $\xi_0(s)$ . It was reported in details the behavior of  $\xi(\sigma, \pi)$  to the varia-

tion of  $G_b$  (Song et al. 2010, 2011). The variation of  $G_b$  results in monopole amplification of S-type contours. Here, we pay attention to the variation of BAO peaks of B-type contours. Thin dash blue curves in the left panel of Fig. 4 represent  $\xi(\sigma, \pi)$  contours with the increment of  $G_b$ . When the broadband shape of spectra is given, the observed BAO tip points mitigate on the same 2D BAO circle. Those are shifted counter-clockwise, while the 2D BAO circle remains unchanged. When  $G_b$  decreases, the BAO tip points move clockwise. Again the 2D BAO circle itself is unchanged.

The anisotropic amplification of S-type contours is generated with the increment of  $G_\Theta$ , because the cross-correlation of density and velocity is a leading term of  $\xi_2(s)$  (Song et al. 2010, 2011). For B-type contours, we observed the invariant 2D BAO circle as well to the variation of  $G_\Theta$ . The BAO tip points move toward the pivot point. The modified B-type contours are presented as thin blue dash contours in the right panel of Fig. 4. The modified 2D BAO circle is presented as thick blue dash curve which is identical to the original circle. When  $G_\Theta$  decreases, the BAO tip points run away from the pivot point on the same circle.

If the correct distances are known, the tip points of BAO peaks form an invariant great circle regardless of galaxy bias and coherent motion.

When  $D_A$  is unknown, the 2D BAO circle becomes uncertain transversely. We decrease  $D_A$  by 10%. The modified  $\xi(\sigma, \pi)$  is presented with thin blue dash contours in the left panel of Fig. 5. The 2D BAO circle is squeezed along the transverse direction. With the increment of  $D_A$ , the circle is stretched along the same direction. When the radial distance varies, the similar behaviors are observed along the  $\pi$  direction. The blue thin dash curves in the right panel of Fig. 5 represent the modified  $\xi(\sigma, \pi)$  when  $H^{-1}$  decreases by 10%. We connect the modified BAO tip points, and find a squeezed circle radially, represented by thick blue dash curve. Again, the radially stretched circle is expected with the increment of  $H^{-1}$ .

Ratio between the observed transverse and radial distances varies with the assumed theoretical models. If the shape of an object is priorly known, then the ratio of the intrinsic transverse and radial distances gives a relation of the observed distance measures of  $D_A$  and  $H^{-1}$ . It is a spirit of Alcock–Paczynski test (Alcock & Paczynski 1979). We show that the 2D BAO circle provides us the object to be invariant to the change of growth functions of density and velocity fields, when the broadband shape of spectra is known. In addition, we show the orthogonal variation of 2D BAO circle to change of  $D_A$  and  $H^{-1}$ , transversely and radially with respect to each other. Therefore, we dub this method as a broadband Alcock–Paczynski test. It is fortunate for us that those BAO peaks are formed at large scales about  $s \sim 100 h^{-1}$  Mpc in which non-perturbative effect on redshift distortions are well described with our theoretical model. Thus, in contrast to the classic method with the broadband but featureless power spectrum or correlation function (e.g., Ballinger, Peacock & Heavens 1996; Matsubara & Suto 1996; Magira, Jing & Suto 2000), the analysis taking account of BAO is expected to be much more powerful.

## 5 RESULTS

In this section, we present the results of broadband Alcock–Paczynski test explained in the previous sections. We present measured values in Table 1, and discuss details below. The quoted errors on the best fit parameters are one sigma, after marginalizing over all other parameters. Throughout the analysis, we adopt the cut-off scales,  $s = 50 h^{-1}$  Mpc and  $\pi = 20 h^{-1}$  Mpc conservatively.

Parameters	Fiducial values	Measurements
$D_A$ ( $h^{-1}$ Mpc)	947.7	$945.1^{+33.0}_{-25.1}$
$H^{-1}$ ( $h^{-1}$ Mpc)	2249.4	$2195.3^{+98.8}_{-130.8}$
$G_b$	–	$1.09^{+0.04}_{-0.07}$
$G_\Theta$	0.43	$0.41^{+0.06}_{-0.05}$
$\sigma_p$ ( $h^{-1}$ Mpc)	–	$5.2^{+2.9}_{-3.9}$

**Table 1.** We present the fiducial and the measured values of ( $G_b, G_\Theta, D_A, H^{-1}, \sigma_p$ ) with the  $1 - \sigma$  confidence level errors. The fiducial values of phenomenological parameters of  $G_b$  and  $\sigma_p$  are not given here.

The angular diameter distance is measured to be  $945.1^{+33.0}_{-25.1}$ . The fiducial value of  $D_A = 947.7 h^{-1}$  Mpc is within  $1 - \sigma$  confidence level of this measured value. The transverse distance is more relevant to the measured  $\xi(\sigma, \pi)$  at  $\pi \rightarrow 0$  bins where the contamination due to non-perturbative effect is minimized. If  $D_A$  were not measured in precision, it would be caused more by the violation of broadband assumption of galaxy density spectra. The  $D_A$  is degenerate more with  $G_b$  than any other observable. The broadband assumption on galaxy density spectra is available when the galaxy bias remains scale-independent above cut-off scales. The precise measurement of  $D_A$  in Table 1 indicates that our assumption is correct.

While the transverse distance can be probed by an another method, the radial distance is a unique outcome of Alcock–Paczynski test. The radial distance is measured to be  $H^{-1} = 2195.3^{+98.8}_{-130.8} h^{-1}$  Mpc, when the fiducial  $H^{-1}$  is  $2249.4 h^{-1}$  Mpc. The fiducial value of  $H^{-1}$  is also well-within  $1 - \sigma$  confidence level. The measurement of  $H^{-1}$  is influenced more by radial bins at  $\mu \rightarrow 1$  where the contamination due to non-perturbative effect is maximized. Therefore, the higher systematic uncertainty is expected to plague through the measured  $H^{-1}$ . Fortunately, it is not severe in our case using BOSS-like simulation. Although  $H^{-1}$  measurement can be biased due to this systematic uncertainty, the effect is buried under the much bigger statistical error. We provide the contour plot of  $D_A$  and  $H^{-1}$  in the left panel of Fig. 6. The fiducial values are represented by a blue square point, the measured values are represented by a black cross point. The inner and outer contours represent the  $1 - \sigma$  and  $2 - \sigma$  confidence levels respectively. The measured values of  $D_A$  and  $H^{-1}$  are located well within  $1 - \sigma$  bound.

The accurate measurement of coherent motion is very important to test modified gravity model cosmologically. The model independent test of general relativity is only available by probing both geometrical perturbations and matter fluctuations separately. While the geometrical perturbations are measured by cosmic shear experiments, the unbiased probe of matter fluctuations is only possible by measuring coherent motions using redshift distortions. It is known that the measurement of coherent motions is difficult, because of non-linear physics contamination. The improved theoretical models of redshift distortions is reported to be an appropriate resolution to overcome this problem for the case of dark matter particles (Song et al. 2013). Here, we show that the coherent growth function  $G_\Theta$  is probed precisely for the case of CMASS samples as well. The  $G_\Theta$  is measured to be  $0.41^{+0.06}_{-0.05}$ , when the fiducial value is  $G_\Theta = 0.43$ . We present it graphically in the right panel of Fig. 6, in order to highlight the precision level. The measured  $G_\Theta$  can be converted into structure formation parameter  $f\sigma_8$  (Song & Percival 2009) as  $f\sigma_8 = 0.42^{+0.07}_{-0.06}$ . The fiducial  $f\sigma_8$  is 0.44. The fractional



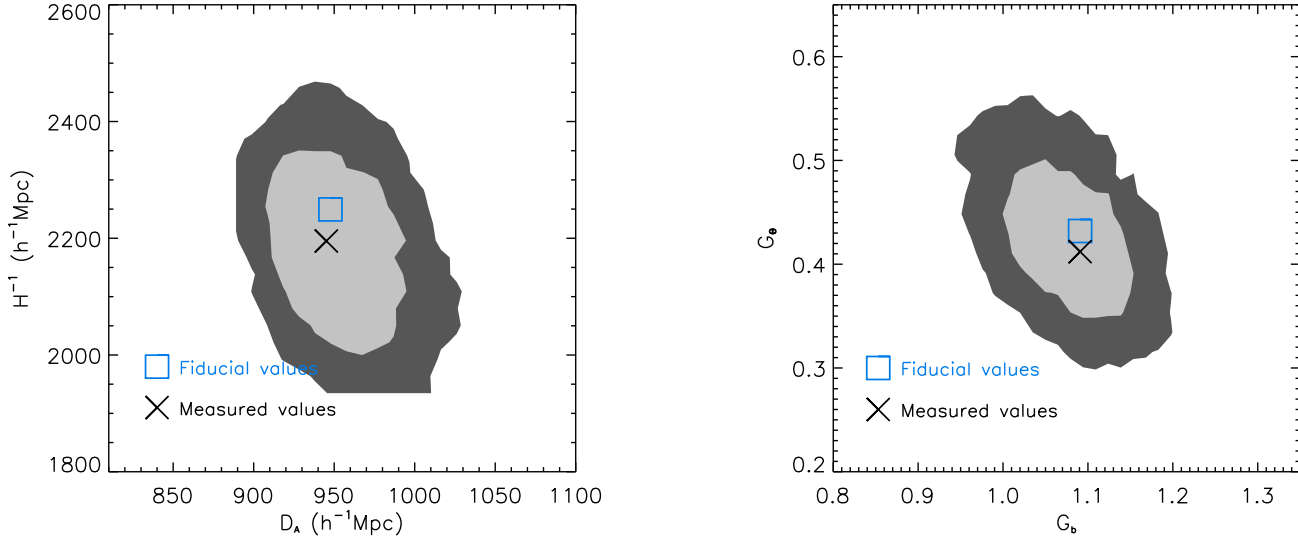


**Figure 6.** (Left panel) The measured  $D_A$  and  $H^{-1}$  are presented. The inner and outer contours represent  $1 - \sigma$  and  $2 - \sigma$  confidence levels respectively. The blue square point represents the fiducial values of  $D_A$  and  $H^{-1}$ , and the black crossed point represents the measured value. (Right panel) The measured  $G_b$  and  $G_\Theta$  are presented. The inner and outer contours represent  $1 - \sigma$  and  $2 - \sigma$  confidence levels respectively. The blue square point represents the fiducial value of  $G_\Theta$ , and the black crossed point represents the measured value.

error to measure  $G_\Theta$  is about 10%. The constraint on coherent motion is poorer by high degeneracy with FoG effect at linear regime. More precise measurement of  $G_\Theta$  is only possible by better understanding of FoG effect.

Unlike observables explained above, there is no fiducial  $G_b$  known. The square point in the right panel of Fig. 6 is presented with the measured  $G_b = 1.09^{+0.04}_{-0.07}$ . The growth function  $G_{\delta_m}$  of dark matter is 0.56 at  $z = 0.57$ . If the galaxy bias is constant, then the measured galaxy bias can be estimated as  $b = 1.91^{+0.08}_{-0.14}$ . The measured galaxy biases are reported in many literature for the same simulation. It ranges from 1.8 to 2, depending on the assumption made in each method. Our galaxy bias is estimated from the decomposed galaxy density spectra which are supposed to be close to spectra in real space. Therefore, it should agree with the value which is measured in real space of the simulation. This value is about  $b = 1.9$  published in Manera et al. (2013). Our measurement agree with it.

Finally, we comment on the FoG parameter  $\sigma_p$ . The measured result is  $5.2^{+2.9}_{-3.9} h^{-1} \text{ Mpc}$ , which is higher than the linear theory estimate of one-dimensional velocity dispersion,  $\sigma_p = 3 h^{-1} \text{ Mpc}$ . The measured velocity dispersion is a factor of 1.5 higher than the linear prediction. The larger value of  $\sigma_p$  might be caused by the higher-order nonlinear correction. Another possibility is the functional form of FoG, which is indeed not precisely known. The discrepancy from Gaussian FoG function may give us impacts on the measured  $\sigma_p$ . If more precise expression on FoG effect is available, then tighter constraints on observables will be made. There are many efforts to formulate non-perturbative effect (Reid & White 2011; Okumura et al. 2012).

## 6 CONCLUSION

Redshift distortions provide a large cosmological object which is appropriate for cosmological tool to measure geometric distances via the Alcock–Paczynski effect. The tip points of BAO peaks on  $\xi(\sigma, \pi)$  clustering function form a great circle called as the 2D BAO circle. When the shape of spectra is pre-determined by CMB experiments, the 2D BAO circle exhibits characteristic anisotropies which remain unchanged to the variations of the unknown galaxy bias and the coherent motion growth function. This feature enables us to probe both transverse and radial distances uniquely. The 2D BAO circle is observed to be altered transversely to the variation of  $D_A$ , and radially to the variation of  $H^{-1}$ . It becomes a reliable large object to test Alcock–Paczynski effect cosmologically. We dub it as a broadband Alcock–Paczynski test in this paper.

The success of this test depends on theoretical models of redshift distortions. We show that BAO peaks of  $\xi(\sigma, \pi)$  are precisely reproduced by the improved redshift distortion model at linear regime. This theoretical model is limited by unknown non-perturbative effect. We ignore the measured  $\xi(\sigma, \pi)$  at small bins in which the contamination caused by non-perturbative effect exceeds more than the first order approximation of Gaussian FoG function. Our cut-off scales are  $s = 50 h^{-1} \text{ Mpc}$  and  $\pi = 20 h^{-1} \text{ Mpc}$  which are enough to include most BAO features, while non-perturbative contamination is safely removed. We reproduce successfully all fiducial values of  $(D_A, H^{-1}, G_\Theta)$  well within  $1 - \sigma$  confidence level. Our results support redshift distortions as a trustable tool to measure key observables to test the dark energy and modify gravity models, even with the conservative bound at linear regime. We note that those constraints will be tightened with better understanding of FoG function in the future.

**ACKNOWLEDGMENTS**

Numerical calculations were performed by using a high performance computing cluster in the Korea Astronomy and Space Science Institute. We would like to thank Marc Manera for providing us with his mock catalogs before publication. This research was partly supported by Republic of Korea WCU grant R32-10130 (T.O.) and a Grant-in-Aid for Scientific Research from the Japan Society for the Promotion of Science (A.T, No. 24540257).

**REFERENCES**

- Alcock C., Paczynski B., 1979, *Nature*, 281, 358  
 Anderson L. et al., 2012, *MNRAS*, 427, 3435  
 Ballinger, W.E. and Peacock, J.A. and Heavens, A.F., 1996, *MNRAS*, 282, 877  
 Bernardeau, F., Crocce, M., Scoccimarro, R., 2008, *Phys.Rev.D78*, 103521  
 Bernardeau, F., Crocce, M., Scoccimarro, R., 2012, *Phys.Rev.D85*, 123519  
 Beutler F., Blake C., Colless M., Jones D. H., Staveley-Smith L., et al., 2012  
 Blake C., Glazebrook K., 2003, *Astrophys.J.*, 594, 665  
 Chuang C.-H., Wang Y., 2012, *Mon.Not.Roy.Astron.Soc.*, 426, 226  
 Drinkwater M. J., Jurek R. J., Blake C., Woods D., Pimblett K. A., et al., 2010, *Mon.Not.Roy.Astron.Soc.*, 401, 1429  
 Eisenstein D. J. et al., 2011, *AJ*, 142, 72  
 Fisher K. B., 1995, *ApJ*, 448, 494  
 Fisher K. B., Scharf C. A., Lahav O., 1994, *MNRAS*, 266, 219  
 Gaztanaga E., Cabre A., Hui L., 2009, *Mon.Not.Roy.Astron.Soc.*, 399, 1663  
 Guzzo L., Pierleoni M., Meneux B., Branchini E., Fevre O. L., et al., 2008, *Nature*, 451, 541  
 Hamilton A. J. S., 1992, *ApJL*, 385, L5  
 Hawkins E., Maddox S., Cole S., Madgwick D., Norberg P., et al., 2003, *Mon.Not.Roy.Astron.Soc.*, 346, 78  
 Hu W., Haiman Z., 2003, *Phys. Rev. D*, 68, 063004  
 Kaiser N., 1987, *Mon.Not.Roy.Astron.Soc.*, 227, 1  
 Kazin E. A., Blanton M. R., Scoccimarro R., McBride C. K., Berlind A. A., 2010, *ApJ*, 719, 1032  
 Kazin E. A., et al., 2010, *Astrophys.J.*, 710, 1444  
 Lahav O., Lilje P. B., Primack J. R., Rees M. J., 1991, *MNRAS*, 251, 128  
 Landy S. D., Szalay A. S., 1993, *ApJ*, 412, 64  
 Lilje P. B., Efstathiou G., 1989, *MNRAS*, 236, 851  
 Lupton R., 1993, *Statistics in theory and practice*  
 Manera M. et al., 2013, *MNRAS*, 428, 1036  
 Matsubara, T., Suto, Y., 1996, *ApJ*, 470, L1  
 Matsubara T., 2004, *ApJ*, 615, 573  
 McGill C., 1990, *MNRAS*, 242, 428  
 Magira, H., Jing, Y.P., Suto, Y., 2000, *ApJ*, 528, 30  
 Okumura T., Matsubara T., Eisenstein D. J., Kayo I., Hikage C., Szalay A. S., Schneider D. P., 2008, *ApJ*, 676, 889  
 Okumura T., Seljak U., McDonald P., Desjacques V., 2012, *JCAP*, 1202, 010  
 Padmanabhan N., White M., 2008, *Phys. Rev. D*, 77, 123540  
 Peacock J. A., Cole S., Norberg P., Baugh C. M., Bland-Hawthorn J., et al., 2001, *Nature*, 410, 169  
 Percival W. J., et al., 2004, *Mon.Not.Roy.Astron.Soc.*, 353, 1201  
 Perlmutter S., et al., 1999, *Astrophys.J.*, 517, 565  
 Reid B. A., Percival W. J., Eisenstein D. J., Verde L., Spergel D. N., et al., 2010, *Mon.Not.Roy.Astron.Soc.*, 404, 60  
 Reid B. A., Samushia L., White M., Percival W. J., Manera M., et al., 2012  
 Reid B. A., White M., 2011, *Mon.Not.Roy.Astron.Soc.*, 417, 1913  
 Riess A. G., et al., 1998, *Astron.J.*, 116, 1009  
 Schlegel D., White M., Eisenstein D., 2009, in *ArXiv Astrophysics e-prints*, Vol. 2010, astro2010: The Astronomy and Astrophysics Decadal Survey, pp. 314+  
 Scoccimarro R., 2004, *Phys.Rev.*, D70, 083007  
 Seo H.-J., Eisenstein D. J., 2003, *Astrophys.J.*, 598, 720  
 Song Y.-S., 2011, *Phys.Rev.*, D83, 103009  
 Song Y.-S., 2013, *Phys.Rev.*, D87, 023005  
 Song Y.-S., Kayo I., 2010, *Mon.Not.Roy.Astron.Soc.*, 407, 1123  
 Song Y.-S., Nishimichi T., Taruya A., Kayo I., 2013, *Phys.Rev.*, D87, 123510  
 Song Y.-S., Percival W. J., 2009, *JCAP*, 0910, 004  
 Song Y.-S., Sabiu C. G., Kayo I., Nichol R. C., 2011, *J. Cosmology Astropart. Phys.*, 5, 20  
 Song Y.-S., Sabiu C. G., Nichol R. C., Miller C. J., 2010, *J. Cosmology Astropart. Phys.*, 1, 25  
 Tang J., Kayo I., Takada M., 2011, *Mon.Not.Roy.Astron.Soc.*, 416, 2291  
 Taruya A., Hiramatsu T., 2008, *Astrophys.J.* 674, 617  
 Taruya A., Bernardeau F., Nishimichi T., Codis S., 2012, *Phys.Rev.*, D86, 103528  
 Taruya A., Nishimichi T., Bernardeau F., 2013, *Phys.Rev.*, D87, 083509  
 Taruya A., Nishimichi T., Saito S., 2010, *Phys.Rev.*, D82, 063522  
 Taruya A., Saito S., Nishimichi T., 2011, *Phys.Rev.*, D83, 103527  
 Tegmark M., et al., 2006, *Phys.Rev.*, D74, 123507  
 Wang Y., 2006, *Astrophys.J.*, 647, 1  
 White M., Song Y.-S., Percival W. J., 2009, *Mon.Not.Roy.Astron.Soc.*, 397, 1348  
 York D. G., et al., 2000, *Astron.J.*, 120, 1579  
 Zehavi I., et al., 2005, *Astrophys.J.*, 630, 1  
 Zhang P., Pan J., Zheng Y., 2013, *Phys.Rev.*, D87, 063526